P H Y S I C A L   R E V I E W   L E T T E R S

Thermally Induced Graphene Rotation on Hexagonal Boron Nitride

Duoming Wang,[1] Guorui Chen,[2] Chaokai Li,[3] Meng Cheng,[1] Wei Yang,[1] Shuang Wu,[1] Guibai Xie,[1] Jing Zhang,[1] Jing Zhao,[1] Xiaobo Lu,[1] Peng Chen,[1] Guole Wang,[1] Jianling Meng,[1] Jian Tang,[1] Rong Yang,[1] Congli He,[1] Donghua Liu,[1] Dongxia Shi,[1] Kenji Watanabe,[4] Takashi Taniguchi,[4] Ji Feng,[3] Yuanbo Zhang,[2] and Guangyu Zhang[1,5,*]

[1]*Beijing National Laboratory for Condensed Matter Physics and Institute of Physics,*
Chinese Academy of Sciences, Beijing 100190, China
[2]*State Key Laboratory of Surface Physics and Department of Physics, Fudan University, Shanghai 200433, China*
[3]*International Center for Quantum Materials, School of Physics, Peking University, Beijing 100871, China*
[4]*National Institute for Materials Science, 1-1 Namiki, Tsukuba 305-0044, Japan*
[5]*Collaborative Innovation Center of Quantum Matter, Beijing 100190, China*

In this Letter, we report the observation of thermally induced rotation of graphene on hexagonal boron nitride (*h*-BN). After the rotation, two thermally stable configurations of graphene on *h*-BN with a relative lattice twisting angle of 0° (most stable) and 30° (metastable), respectively, were found. Graphene on *h*-BN with a twisting angle below (above) a critical angle of $\sim 12 \pm 2°$ tends to rotate towards 0° (30°) at a temperature of $>100\,°C$, which is in line with our theoretical simulations. In addition, by manipulating the annealing temperature and the flake sizes of graphene, moiré superlattices with large spatial periods of graphene on *h*-BN are achieved. Our studies provide a detailed understanding of the thermodynamic properties of graphene on *h*-BN and a feasible approach to obtaining van der Waals heterostructures with aligned lattices.

van der Waals (vdW) interactions in layered materials such as graphite, hexagonal boron nitride (*h*-BN), molybdenum, or tungsten disulfides are relatively weak, enabling the easy change of the relative motion of individual layers upon external forces. As a consequence, these bulk materials can be used for solid lubricants and exfoliation of monolayer flakes in order to obtain 2D atomic crystals. Moreover, the interlayer vdW interaction also depends sensitively on the relative lattice orientations of two neighboring layers. It has been proposed that superlubricity could appear at an incommensurate interface [1–11]. Such a superlubricity effect would be more prominent for vdW heterostructures with lattice mismatch [6,10]. Considering even lower interlayer friction in the vdW heterostructures, their thermal stability would be different from the existing materials. Graphene on *h*-BN has recently attracted great interest since the pioneering work of Dean *et al.* [Ref. [12]. It has been shown that *h*-BN emerges as an excellent substrate for graphene to approach its intrinsic properties and reshape its band structure through a periodic moiré superlattice modulation as well [12–25]. While most of the recent research has focused on the electrical or optical properties, the thermal stability of graphene on *h*-BN has not yet been investigated experimentally. Taking advantage of the latest progress of stacking different 2D atomic crystals into vdW heterostructures, we now can address such thermal stability issues.

In this work, graphene on *h*-BN heterostructures were fabricated by a mechanical transfer process [12]. *h*-BN flakes were first prepared by mechanical exfoliation of *h*-BN

crystals onto the 300 nm SiO_2/Si substrate. Then graphene was mechanically transferred onto *h*-BN. The structure is shown schematically in Fig. 1(a). Note that we did not apply any orientational control and our as-fabricated heterostructures have random stacking orientations between graphene and *h*-BN. In most cases, as-transferred graphene partially overlaps with the *h*-BN substrate. The remaining graphene is
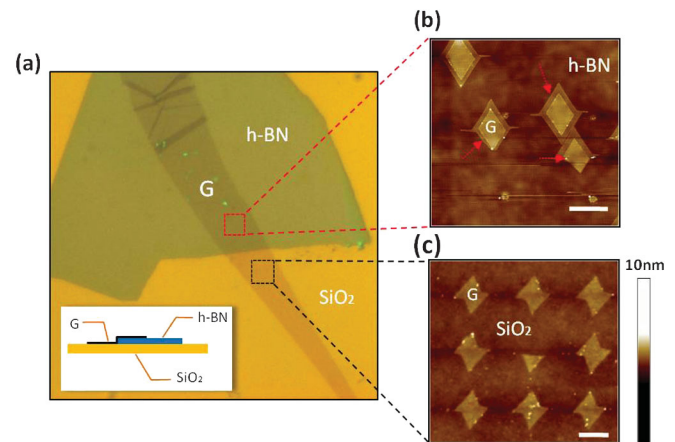

FIG. 1.   As-transferred graphene and as-fabricated graphene flake arrays on *h*-BN and SiO_2. (a) Optical image of mechanically transferred graphene with part (top) on *h*-BN and part (bottom) on SiO_2. Inset: side view schematic diagram. (b) and (c) AFM morphology images of as-fabricated graphene flake arrays on *h*-BN [(b)] and SiO_2 [(c)], separately captured from red and black square areas in (a). The scale bars in (b) and (c) are 500 nm.

126101-1

anchored on the SiO_2 substrate. In order to isolate graphene from the SiO_2 substrate while allowing its rotation on the h-BN surface, the graphene is separated into isolated flakes via a self-aligned patterning process [26,27]. In this process, electron beam lithography and oxygen-plasma etching were first applied to pattern an array of circular holes in graphene as artificial defects. Subsequently, anisotropic hydrogen plasma etching was carried out at a temperature of 450 °C to separate graphene into isolated flakes. Note that this anisotropic etching enables us to tailor graphene without damaging the h-BN underneath. After the anisotropic etching, zigzag edges were formed [26,27], which is an important mark for us to determine the rotation angle of graphene on h-BN.

Figures 1(b) and 1(c) show atomic force microscope (AFM) images of a typical large graphene domain on a SiO_2 and h-BN surface after indiscriminate patterning, respectively. Since graphene on a rough SiO_2 surface is very stable after the patterning process [26,27], it provides a reference for the orientation of graphene on h-BN. We can clearly see that those graphene flakes on h-BN rotate and translocate after patterning at a temperature of 450 °C. Red arrows in Fig. 1(b) show the possible translation trace of each flake. This rotation is attributed to the thermal annealing activation, as will be confirmed below. We examined many such samples and found that there are only two stable configurations of G/h-BN with relative lattice twisting angles θ close to 30° [Fig. 2(a)] and 0° [Fig. 2(b)] after annealing. The ~0° twisting angle can be confirmed by the enlarged AFM image [Fig. 2(d)] with moiré patterns at a spatial period of approximately 15 nm. Note that the orientation of the moiré pattern is parallel to the zigzag edge of the graphene flake, which further verifies the nature of the 0° twisting angle [19,20]. For the graphene

on h-BN with a 30° twisting angle, the moiré pattern exhibits a small period of approximately 0.5 nm, and thus is not visible under AFM imaging [Fig. 2(c)]. Thus, we need to further rotate the object to ~0° by AFM tip mechanical manipulation [28]. Manipulation of graphene flakes on h-BN is carried out in an AFM (MultiMode IIId, Veeco Instruments, Inc.) with standard p-doped silicon tips (spring constant, 20–80 N/m; tip radius, ~20 nm) (see Supplemental Material [29]). In this way, the ~30° twisting angle can be extrapolated. Figures 2(e) (30°) and 2(f) (0°) reveal corresponding stacking configurations at the atomic level. The same approach was also applied to graphene on graphite and we found similar bistable behavior, as demonstrated in Figs. 2(g) (30°) and 2(h) (0°). Note that the lattice twisting angles can be directly defined from the edge alignment for graphene on graphite since the edges are all zigzag edges. We speculate that this thermal-induced rotation phenomenon should also be observed in other vdW heterostructures, such as MoS_2/h-BN and MoS_2/graphene.

The 0°-twisted G/h-BN is believed to be the most stable configuration since it is difficult to rotate graphene further, even by AFM tip mechanical manipulation. To further study this rotation process, the 30°-twisted G/h-BN samples are selected. These samples were first rotated by the AFM tip into certain angles at ambient conditions, followed by additional thermal annealing at an elevated temperature of 400 °C in order to enable the rotation. Thermal annealing was carried out in a vacuum chamber with Ar as a protection gas. Two examples are shown in Fig. 3. With an annealing time of one hour, 20°-twisted graphene on h-BN tends to rotate back to ~30° [Fig. 3(c)], whereas 8°-twisted graphene on h-BN tends to rotate to ~0° [Fig. 3(f)]. Figure 3(g) shows the superlattice morphology of the square area in Fig. 3(f), revealing a moiré pattern period
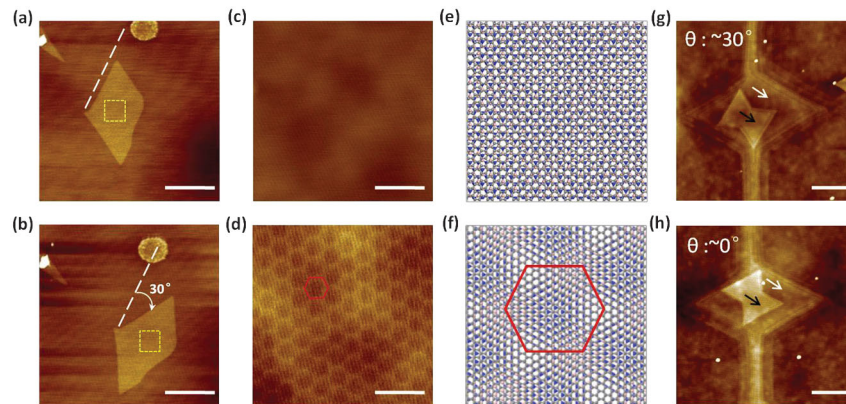

FIG. 2. Stable configurations of G/h-BN and graphene on graphite stackings. (a) and (b) AFM images of two G/h-BN stacking configurations with relative angle difference of 30°. Sample in (a) is as-prepared sample as that in Fig. 1(b). Flake in (b) results from clockwise rotation of the flake in a by 30° in a manipulation process. The scale bars in (a) and (b) are 400 nm. (c) and (d) Englarged AFM images of yellow square areas in (a) and (b), respectively. The unit cell of the moiré pattern is marked by a red hexagon. The scale bars in (c) and (d) are 40 nm. (e) and (f) Schematic maps of atomic structures in (c) and (d), respectively. Mismatch in lattice between graphene and h-BN is exaggerated to 10%. (g) and (h) AFM images of graphene on graphite stacking configurations with relative angle θ: ~30° and ~0°, respectively. Graphene on top and graphite at bottom are denoted by black and white arrows, respectively. The scale bars in (g) and (h) are 400 nm.
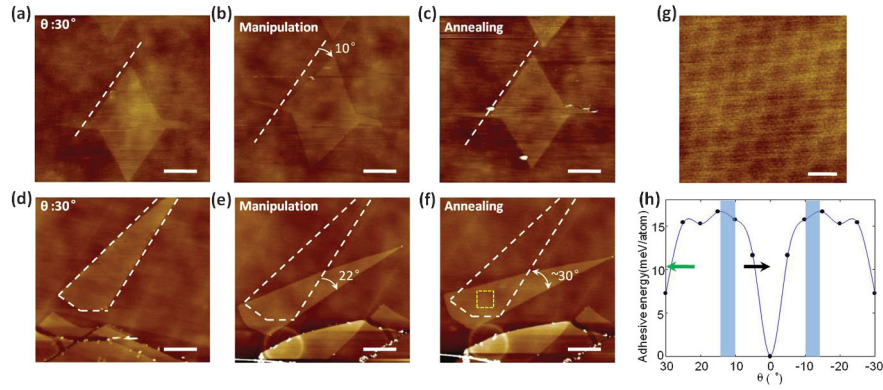
FIG. 3. Unstable configurations and thermal-induced rotations of graphene on h-BN. (a) and (d) AFM images of as-prepared 30°-twisted G/h-BN samples. (b) and (e) Unstable configurations resulting from manipulations [clockwise rotation of 10° (b) and 22° (e), respectively] on corresponding graphene flake in (a) and (d). (c) and (f) Configurations after annealing treatment (400 °C for 1 h) on samples shown in (b) and (e), respectively. In (a)–(f), dashed white lines mark the edges of graphene in as-prepared 30°-twisted G/h-BN samples and the scale bars are 400 nm. (g) Enlarged AFM image of the yellow square area in (f). The scale bar in (g) is 10 nm. (h) Adhesive energy of G/h-BN stacking as a function of stacking angles from first principles simulation. The energy of the 0° configuration is set to zero. The blue curve is a fit of the energy. Green and black arrows denote the thermal-induced rotations to 30° [evolution from (b) to (c)] and ~0° [evolution from (e) to (f)], respectively. The two strips show the experimentally estimated position of energy barrier ($12 \pm 2°$).

of ~12.3 nm, which corresponds to a twisting angle of ~0.5°. Tens of samples are examined in this Letter and it is established that this thermal-induced rotation phenomenon is universal at elevated temperatures, i.e., $T > 100\,°C$. Note that, at room temperature, we did not observe any rotation of these graphene flakes for at least one month.

We also found a critical twisting angle of $\theta_c \sim 12 \pm 2°$ [denoted by strips in Fig. 3(h)] between graphene and h-BN. During thermal annealing, when $\theta < \theta_c$, the rotation is toward 0°; alternatively, when $\theta > \theta_c$, the rotation is toward 30°. This bidirectional rotation suggests an energy barrier lying between these two stable stacking configurations. First-principles simulation was thus carried out to investigate the adhesive energy of the G/h-BN structure as a function of θ (see Supplemental Material [29]). The calculated results are shown in Fig. 3(h). Two major features are revealed here. First, two energy minima are observed at 0° and 30° and the smallest adhesive energy appears at 0°, suggesting that the 0° configuration is the most stable; second, an energy maxima is close to a critical angle of $\theta_c \sim 15°$, which agrees with the experimentally observed $\theta_c \sim 12 \pm 2°$. Furthermore, the structural relaxation was also performed with two different configurations at 0° and 30°. After the relaxation, the overall twisting angles of 0° and 30° remain unchanged, suggesting that these two configurations are local energy minima. Other configurations all exhibit overall relative rotations, suggesting that these geometries are not stable. The simulation results are in line with our experimental data shown above.

Graphene flakes could also translocate on h-BN during the thermal annealing, as seen in Fig. 1(b). As discussed above, the 0°-twisted G/h-BN is the most thermally stable

configuration; therefore, either rotation or translocation is difficult to achieve even by AFM tip manipulation. To understand this phenomenon, further simulations are carried out. Here, the substrate is treated as a potential energy landscape in the Tomlinson model and Frenkel-Kontorova model for wearless sliding friction. Figure 4(a) shows the dependence of the sliding energy corrugation (ΔE) of G/h-BN with different θ on the graphene translocation distance. For simplicity, translocation only along zigzag (green) and armchair (blue) directions of h-BN is considered. The schematic map in the inset of Fig. 4(a) shows the translocation of graphene for 0°-twisted G/h-BN. The simulation results show that the sliding energy corrugation around $\theta = 0°$ is much larger, suggesting a very large interface friction near $\theta = 0°$. Energy corrugation creates an obvious decrement around the energy barrier [denoted by the dashed line in Fig. 4(a)], which indicates that the friction for rotation towards 30° is much smaller than that towards 0°. Experimentally, we indeed observed that the rotation toward 30° is much faster than that toward 0° as shown in Fig. 4(b). Rotation rates extracted from Fig. 4(b) are 12°/h for rotation towards 30° and 1°/h for rotation towards 0°, respectively. Note here that the annealing temperatures are both 200 °C and the sizes of graphene flakes are almost identical.

As shown in previous studies, G/h-BN with a large moiré superlattice wavelength (λ), i.e., near 0°-twisted structures, has gained particular interest [15–24]. The thermal annealing process thus provides a facile and efficient approach for the fabrication of such large wavelength moiré superlattices. As shown below, the annealing temperature, annealing durations, and the size of graphene flakes are important factors to obtain such slightly misaligned graphene flakes on
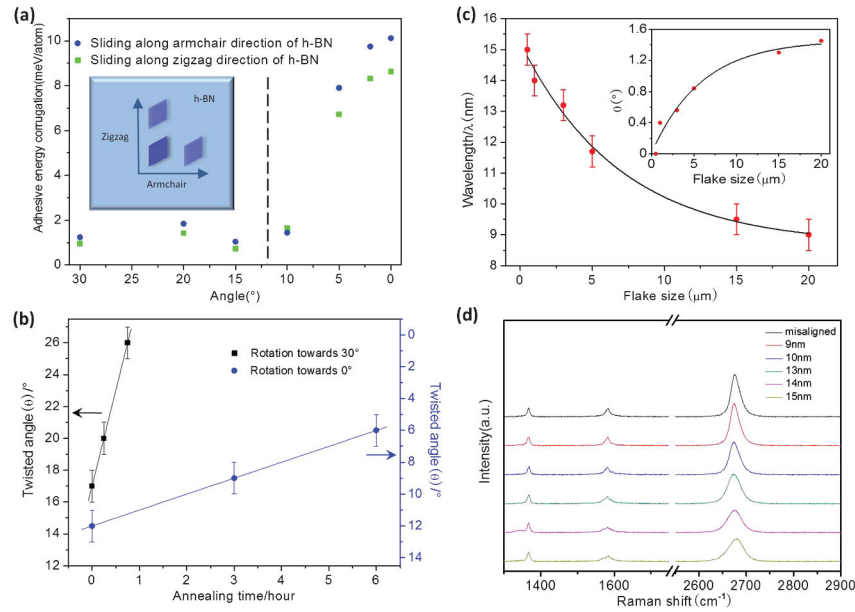
FIG. 4. Sliding energy corrugation-interface friction and the dependences of graphene rotation on annealing time and flake size.
(a) Sliding energy corrugation (adhesive energy corrugation when graphene translates on h-BN) from first principles simulation plotted
against twisted angle. Blue and green dots separately correspond to sliding along armchair and zigzag directions of the underlying h-BN.
The dashed line shows the experimentally estimated position of the energy barrier (12°). Inset: schematic map of graphene translation
along the zigzag and armchair directions for 0°-twisted G/h-BN. (b) Typical relationships between the twisted angle and annealing time
in rotations towards 30° and 0°. Two consecutive annealing processes (at 200 °C) were carried out. The black and blue lines are linear
fits. The error bars are ±1°. (c) Relationship between wavelength of obtained superlattice (near 0°) and size of graphene flake. The
annealing temperature is 1000 °C. The black curve is a fit. The error bars are ±0.5 nm. Inset: Relationship between twisting angle (θ)
and size of graphene flake. (d) Raman spectra of superlattices with a different wavelength.

h-BN. We found that the higher annealing temperature,
longer annealing durations, and smaller graphene flakes
can promote the graphene rotation on h-BN to approach 0°
twisting angle. For the flake shown in Fig. 3(f), λ increases
from 12.3 to 13.2 nm after the annealing temperature is
further increased from 400 to 1000 °C. The holding time at
the preset annealing temperature is 1 h. To reduce graphene
ripples possibly induced by annealing, heating and cooling
rates were set at 10 °C/ min. Figure 4(c) shows the measured
λ for a series of samples with different flake sizes, revealing
that smaller graphene flakes tend to approach a twisting
angle of 0° [inset of Fig. 4(c)]. This relationship can be

fitted by an exponential decay curve, written as $\lambda(\text{nm}) =
6.5 \exp(-L/7) + 8.7$ [where L (μm) is the length of the
graphene flake], although we do not quite understand the
physical origin of this formula. Figure 4(d) shows the Raman
spectra of a series of as-made G/h-BN samples with a small
twisting angle. The 2D Raman spectral peak of monolayer
graphene on h-BN shows a gradual broadening when the
twisting angle approaches 0°. The full width at half-
maximum (FWHM) of the 2D peak follows a rule of
FWHM(2D) = 2.5λ (Fig. S5 [29]), which is consistent with
previous results [21]. The Raman spectra were acquired
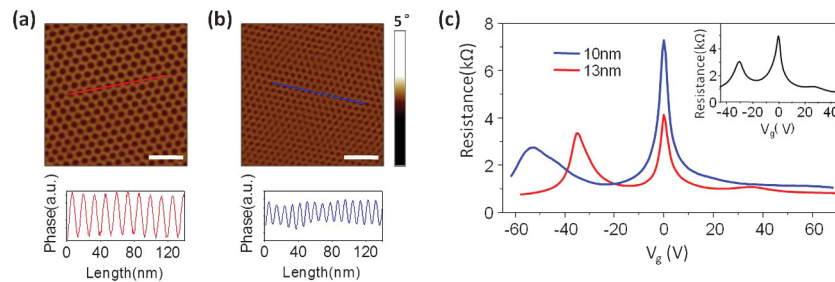using a micro-Raman microscope (Horiba Jobin Yvon

FIG. 5. Moiré patterns in phase diagram and electrical measurements. (a) and (b) Fast Fourier Transform filtered phase diagram of
G/h-BN superlattices with λ: 13 nm [(a)] and 10 nm [(b)], respectively. Lower parts are the profiles along the red and blue lines. The
scale bars in (a) and (b) are 40 nm. (c) Transfer characteristics of samples shown in (a) and (b). Inset: Transfer curve of epitaxial graphene
on h-BN with precise lattice alignment ($\theta = 0°$).

LabRAM HR-800) with an excitation laser wavelength of 532 nm, a power of 10 mW, and a beam spot size of 1 μm.

Based on the G/h-BN structures with different λ, we thus fabricated field effect transistor (FET) devices to explore their electrical transport properties. Graphene FET devices were fabricated following the standard lithography process and subsequent metal deposition of Pd/Au (10 nm/50 nm) by e-beam evaporation. The electrical transport measurements of the devices were carried out at liquid nitrogen temperature (77 K) in a four-point probe station by a semiconductor parameter analyzer (Agilent 4156c). Figures 5(a) and 5(b) show the fast-Fourier-transform filtered phase images of two samples with $\lambda \approx 13$ and $\lambda \approx 10$ nm, respectively (see Supplemental Material [29]). Note that the phase profile of the superlattice shows the same periodicity as that in the height images. Figure 5(c) shows the resistance (R) of the two devices under a static gate (V_g) modulation from −60 to 60 V. R-V_g curves show clearly the appearance of additional Dirac points, which are called superlattice Dirac points (SDPs). The R-V_g curve for the epitaxial grown graphene on h-BN, as a control sample in which the twisting angle is precisely at $\theta = 0°$ [19], is shown in the inset of Fig. 5(c). It is found that ΔV_g are 54, 38, and 30 V, for 10, 13, and 15 nm samples, respectively. Here, ΔV_g is the gate voltage difference between SDP and DP. The positions of SDPs are directly related to λ as expected and are adequately accounted for by the equation (refer to our previous analysis described in Ref. [19] for more details).

$$\Delta V_g = 4\pi e/(3\lambda^{2*}C_g), \qquad (1)$$

Here, C_g is the capacitance of the device, which is ∼10.2 nF/cm^2 with the thicknesses of the h-BN flakes and SiO$_2$ substrates are ∼30 and 300 nm, respectively.

In summary, we observed the rotation of graphene on h-BN by thermal annealing at elevated temperatures. Two thermally stable configurations of graphene on h-BN, with a relative lattice twisting angle of 0° and 30°, respectively, were found. Graphene on h-BN with a twisting angle below (above) a critical angle of $\theta_c \sim 12 \pm 2°$ tends to rotate towards 0° (30°) at a temperature above 100 °C. Moreover, by controlling the annealing temperature and flake sizes of graphene, large wavelength superlattices can be achieved efficiently. The experimental results reported in this Letter agree perfectly with our simulation results. Our studies provide a better understanding of the thermodynamic properties of graphene on h-BN and lead directly to a feasible approach to obtaining van der Waals heterostructures with aligned lattices.

———————

*To whom all correspondence should be addressed.
gyzhang@aphy.iphy.ac.cn

[1] M. Dienwiebel, G. S. Verhoeven, N. Pradeep, J. W. M. Frenken, J. A. Heimberg, and H. W. Zandbergen, Phys. Rev. Lett. **92**, 126101 (2004).

[2] Y. Liu, F. Grey, and Q. Zheng, Sci. Rep. **4**, 4875 (2014).

[3] I. V. Lebedeva, A. A. Knizhnik, A. M. Popov, O. V. Ershova, Y. E. Lozovik, and B. V. Potapkin, Phys. Rev. B **82**, 155460 (2010).

[4] Q. S. Zheng, B. Jiang, L. S. P. Liu, Y. X. Wang, L. Lu, Q. K. Xue, J. Zhu, Q. Jiang, S. Wang, and L. M. Peng, Phys. Rev. Lett. **100**, 067205 (2008).

[5] Z. Liu, J. Yang, F. Grey, J. Z. Liu, Y. Liu, Y. Wang, Y. Yang, Y. Cheng, and Q. Zheng, Phys. Rev. Lett. **108**, 205503 (2012).

[6] L. F. Wang, T. B. Ma, Y. Z. Hu, Q. Zheng, H. Wang, and J. Luo, Nanotechnology **25**, 385701 (2014).

[7] Z. Xu, X. Li, B. I. Yakobson, and F. Ding, Nanoscale **5**, 6736 (2013).

[8] X. Feng, S. Kwon, J. Y. Park, and M. Salmeron, ACS Nano **7**, 1718 (2013).

[9] O. Hod, Phys. Rev. B **86**, 075444 (2012).

[10] I. Leven, D. Krepel, O. Shemesh, and O. Hod, J. Phys. Chem. Lett. **4**, 115 (2013).

[11] A. E. Filippov, M. Dienwiebel, J. W. M. Frenken, J. Klafter, and M. Urbakh, Phys. Rev. Lett. **100**, 046102 (2008).

[12] C. R. Dean, A. F. Young, I. Meric, C. Lee, L. Wang, S. Sorgenfrei, K. Watanabe, T. Taniguchi, P. Kim, K. L. Shepard, and J. Hone, Nat. Nanotechnol. **5**, 722 (2010).

[13] R. Decker, Y. Wang, V. W. Brar, W. Regan, H. Tsai, Q. Wu, W. Gannett, A. Zettl, and M. F. Crommie, Nano Lett. **11**, 2291 (2011).

[14] J. Xue, J. Sanchez-Yamagishi, D. Bulmash, P. Jacquod, A. Deshpande, K. Watanabe, T. Taniguchi, P. J. Herrero, and B. J. LeRoy, Nat. Mater. **10**, 282 (2011).

[15] M. Yankowitz, J. Xue, D. Cormode, J. D. Sanchez-Yamagishi, K. Watanabe, T. Taniguchi, P. J. Herrero, P. Jacquod, and B. J. LeRoy, Nat. Phys. **8**, 382 (2012).

[16] L. A. Ponomarenko, R. V. Gorbachev, G. L. Yu, D. C. Elias, R. Jalil, A. A. Patel, A. Mishchenko, A. S. Mayorov, C. R. Woods, J. R. Wallbank, M. Mucha-Kruczynski, B. A. Piot, M. Potemski, I. V. Grigorieva, K. S. Novoselov, F. Guinea, V. I. Fal'ko, and A. K. Geim, Nature (London) **497**, 594 (2013).

[17] C. R. Dean, L. Wang, P. Maher, C. Forsythe, F. Ghahari, Y. Gao, J. Katoch, M. Ishigami, P. Moon, M. Koshino, T. Taniguchi, K. Watanabe, K. L. Shepard, J. Hone, and P. Kim, Nature (London) **497**, 598 (2013).

[18] B. Hunt, J. D. Sanchez-Yamagishi, A. F. Young, M. Yankowitz, B. J. LeRoy, K. Watanabe, T. Taniguchi, P. Moon, M. Koshino, P. Jarillo-Herrero, and R. C. Ashoori, Science **340**, 1427 (2013).

[19] W. Yang, G. Chen, Z. Shi, C. Liu, L. Zhang, G. Xie, M. Cheng, D. Wang, R. Yang, D. Shi, K. Watanabe, T. Taniguchi, Y. Yao, Y. Zhang, and G. Zhang, Nat. Mater. **12**, 792 (2013).

[20] S. Tang, H. Wang, Y. Zhang, A. Li, H. Xie, X. Liu, L. Liu, T. Li, F. Huang, X. Xie, and M. Jiang, Sci. Rep. **3**, 2666 (2013).

[21] A. Eckmann, J. Park, H. Yang, D. Elias, A. S. Mayorov, G. Yu, R. Jalil, K. S. Novoselov, R. V. Gorbachev, M. Lazzeri, A. K. Geim, and C. Casiraghi, Nano Lett. **13**, 5242 (2013).

[22] Z. Chen, Z. Shi, W. Yang, X. Lu, Y. Lai, H. Yan, F. Wang, G. Zhang, and Z. Li, Nat. Commun. **5**, 4661 (2014).

[23] C. R. Woods, L. Britnell, A. Eckmann, R. S. Ma, J. C. Lu, H. M. Guo, X. Lin, G. L. Yu, Y. Cao, R. V. Gorbachev, A. V. Kretinin, J. Park, L. A. Ponomarenko, M. I. Katsnelson, Y. N. Gornostyrev, K. Watanabe, T. Taniguchi, C. Casiraghi, H. J. Gao, A. K. Geim, and K. S. Novoselov, Nat. Phys. **10**, 451 (2014).

[24] Z. Shi, C. Jin, W. Yang, L. Ju, J. Horng, X. Lu, H. A. Bechtel, M. C. Martin, D. Y. Fu, J. Q. Wu, K. Watanabe, T. Taniguchi, Y. Zhang, X. D. Bai, E. Wang, G. Zhang, and F. Wang, Nat. Phys. **10**, 743 (2014).

[25] S. Tang, H. Wang, H. S. Wang, Q. Sun, X. Zhang, C. Cong, H. Xie, X. Liu, X. Zhou, F. Huang, X. Chen, T. Yu, F. Ding, X. Xie, and M. Jiang, Nat. Commun. **6**, 6466 (2015).

[26] R. Yang, L. Zhang, Y. Wang, Z. Shi, D. Shi, H. Gao, E. Wang, and G. Zhang, Adv. Mater. **22**, 4014 (2010).

[27] Z. Shi, R. Yang, L. Zhang, Y. Wang, D. Liu, D. Shi, E. Wang, and G. Zhang, Adv. Mater. **23**, 3061 (2011).

[28] M. Cheng, D. Wang, Z. Sun, J. Zhao, R. Yang, G. Wang, W. Yang, G. Xie, J. Zhang, P. Chen, C. He, D. Liu, L. Xu, D. Shi, E. Wang, and G. Zhang, ACS Nano **8**, 3955 (2014).

[29] See Supplemental Material at http://link.aps.org/supplemental/10.1103/PhysRevLett.116.126101, which includes Refs. [30–35], for more rotation and translation details for monolayer and few layer graphene flakes on h-BN, more Raman spectra and AFM diagrams of superlattice with different wavelengths, and simulation methods.

[30] P. Hohenberg and W. Kohn, Phys. Rev. **136**, B864 (1964).

[31] W. Kohn and L. J. Sham, Phys. Rev. **140**, A1133 (1965).

[32] G. Kresse and J. Furthmuller, Phys. Rev. B **54**, 11169 (1996).

[33] J. Klimes, D. R. Bowler, and A. Michaelides, J. Phys. Condens. Matter **22**, 022201 (2010).

[34] J. Klimes, D. R. Bowler, and A. Michaelides, Phys. Rev. B **83**, 195131 (2011).

[35] G. Kresse and D. Joubert, Phys. Rev. B **59**, 1758 (1999).